Drag reduction using wrinkled surfaces in high Reynolds number laminar boundary layer flows

Citation: Raayai-Ardakani, Shabnam and Gareth H. McKinley. "Drag Reduction Using Wrinkled Surfaces in High Reynolds Number Laminar Boundary Layer Flows." Physics of Fluids 29, 9 (September 2017): 093605

As Published: http://dx.doi.org/10.1063/1.4995566

Publisher: American Institute of Physics (AIP)

Persistent URL: http://hdl.handle.net/1721.1/119866

Version: Author's final manuscript: final author's manuscript post peer review, without publisher's formatting or copy editing

Drag Reduction Using Wrinkled Surfaces in High Reynolds Number Laminar Boundary Layer Flows

Shabnam Raayai-Ardakani[1, a)] and Gareth McKinley[1, b)]
Department of Mechanical Engineering, Massachusetts Institute of Technology, Cambridge, Massachusetts, 02139, USA

(Dated: 30 August 2017)

Inspired by the design of the ribbed structure of shark skin, passive drag reduction methods using stream-wise riblet surfaces have previously been developed and tested over a wide range of flow conditions. Such textures aligned in the flow direction have been shown to be able to reduce skin friction drag by $4-8\%$. Here, we explore the effects of periodic sinusoidal riblet surfaces aligned in the flow direction (also known as a "wrinkled" texture) on the evolution of a laminar boundary layer flow. Using numerical analysis with the open source CFD solver OpenFOAM, boundary layer flow over sinusoidal wrinkled plates with a range of wavelength to plate length ratios (λ/L), aspect ratios ($2A/\lambda$), and inlet velocities are examined. It is shown that in the laminar boundary layer regime the riblets are able to retard the viscous flow inside the grooves creating a cushion of stagnant fluid which the high speed fluid above can partially slide over, thus reducing the shear stress inside the grooves and the total integrated viscous drag force on the plate. Additionally, we explore how the boundary layer thickness, local average shear stress distribution, and total drag force on the wrinkled plate vary with the aspect ratio of the riblets as well as the length of the plate. We show that riblets with an aspect ratio of close to unity lead to the highest reduction in the total drag, and that because of the interplay between the local stress distribution on the plate and stream-wise evolution of the boundary layer the plate has to exceed a critical length to give a net decrease in the total drag force.

Keywords: Drag Reduction, Riblets, Boundary Layers, Laminar, OpenFOAM

I. INTRODUCTION

The concept of achieving frictional drag reduction at high Reynolds numbers using riblets was first introduced close to 40 years ago[43]. In this approach to skin friction reduction, surfaces textured with stream-wise riblets (aligned in the flow direction) are used to modify the local flow near the textured surface. Previous experimental measurements and numerical calculations have shown a possibility of achieving up to 10 % reduction in the total frictional drag on an immersed and textured surface[38].

The concepts underpinning riblet-based drag reduction were originally motivated by a number of independent ideas: First, biological observation of fine ridges aligned in the flow direction on the denticles of fast-swimming sharks (which are closely packed all over the sharks' body) raised the possibility of achieving drag reduction using stream-wise grooves.[2,4,11,42] Second, it was suggested that riblets or stream-wise grooved textures could constrain the growth of turbulent structures and reduce the Reynolds shear stress near the wall by choosing physical rib sizes smaller than the radius of the vortices.[8,10,18,26,42] Independent DNS calculations and experimental measurements in turbulent boundary layer and channel flows for various Reynolds numbers in the range of $Re_L \approx 3\times10^4 - 8\times10^5$ have shown that the diameter of the stream-wise vortical structures near the wall have values of between 10 and 44 δ^* and the mean spacing of these structures is about 100 δ^*.[24,25,33] Here

[a)] shraayai@mit.edu
[b)] gareth@mit.edu

the Reynolds number is defined as $Re_L = \rho V L/\mu$ where ρ and μ are the fluid density and viscosity, V is the characteristic velocity, and L the characteristic length, and the viscous length scale δ^* is defined as ν/v^* where $v^* = \sqrt{\tau_w/\rho}$ and τ_w is the magnitude of the wall shear stress.

Third, advances in techniques used to manufacture pipes with straight or spiral fins lead to new experiments in 1970s on the heat transfer of turbulent flows past walls with stream-wise fins, and sharp internal corners (i.e. rectangular ducts and conduits). Experimentally, it has been observed that the secondary flow structures that develop inside the corners of non-circular ducts, and at the base of the fins (the intersection of the fins with the conduit walls) result in a reduced local shear stress.[17,22,42] In addition, it was shown that such corners can weaken the spatial development of the three dimensional flow inside the corner by limiting the span-wise component of the velocity, therefore resulting in a local re-laminarization of flow inside the corners.[34,42] Thus, it was hypothesised that walls with periodic textures aligned in the stream-wise directions (such as riblets) that contributed a large number of independent corner regions could perform in a similar manner.[17,22,34,42]

Independently, in recent decades, new developments in soft materials research have demonstrated the possibility of creating surfaces with various types of wrinkled textures in the forms of sinusoidal periodic and non-periodic wrinkles and herringbone patterns using hyper-elastic materials.[7,31,45] Using 3D printing methods, Wen et al. have used micro-CT scans of a shortfin mako shark to replicate shark denticles. They arrayed the printed denticles linearly on a flexible substrate that was then immersed in a tow tank used for hydrodynamic testing, including net drag force measurements. Their results showed drag reduction for channel Reynolds number larger than $Re_L > 9.6 \times 10^4$ and for denticles with rib spacing of 51 μm and rib heights between $11 - 21$ μm.[44] With the advances in our understanding of the tunability of the wavelength and amplitude of textured surfaces with geometric, dynamic and material parameters, it is also of interest to investigate the possibility of using such surfaces for applications such as smart adhesion[6], and flow control. Terwagne et al. have recently used dimpling patterns of wavelength of 4.37 mm and average dimple depth of between $0 - 0.8$ mm on spherical surfaces of 20 mm radius and showed the potential of dynamically controlling the total drag for Reynolds numbers between $5 \times 10^3 - 10^5$.[35]

In order, to understand the integrated effect of the riblets on the structure of a viscous boundary layer, it is important to first systematically unravel how the laminar boundary layer spatially evolves over riblet textured surfaces prior to the transition to turbulence, and whether changes in the corresponding laminar flow evolution could lead to an increase or reduction in the total drag force on the surface compared to a flat plate. In this paper, we explore the changes induced by periodic sinusoidal wrinkles on a spatially developing laminar viscous boundary layer flow. We study the systematic changes in velocity profiles, pressure distribution and the resulting local changes in the boundary layer thickness and the shear stress distribution along the length and breadth of the textured plate. By understanding each of these local kinematic and dynamical changes we can then ultimately evaluate the effect of the riblets on the total integrated viscous drag force. In general, unperturbed boundary layers over plates remain laminar up to Reynolds numbers close to 5×10^5 and then naturally transition to turbulence.[32] Note we also recognize that boundary layers can be tripped to transition at earlier Reynolds numbers, resulting in an increase in the total frictional drag force, however this is not the focus of this study.[1,28]

This paper is organized as follows: in section II, we discuss the numerical method used in the research combined with a grid resolution and benchmark study of flat plate boundary layer. Then in section III, the primary results of the numerical study are presented; first we discuss the evolution of the velocity profiles along the boundary layer that develops over periodic riblet surfaces as well as the pressure distribution in the stream-wise direction. Then we discuss the effect of wrinkles of various aspect ratio on the thickness of the boundary layer, and lastly we explore the effect of the riblets on changes in the local shear stress distribution along the length of the plate as well as on the total integrated frictional drag over riblet surfaces with various aspect ratios.

II. METHOD

Our goal is to solve the full steady-state Navier-Stokes equations for the three velocity components (u, v, w) and the pressure (p) distribution in the laminar viscous boundary layer that develops over different textured plate geometries. In the present study the numerical simulations are carried out using the finite volume method (FVM), with the SIMPLE algorithm (Semi Implicit Method for Pressure Linked Equations)[37]. The SIMPLE algorithm is widely used for steady state problems with velocity and pressure coupling and was first introduced by Patankar and Spalding in 1972[30]. In this algorithm initial guesses for the velocity and pressure components are provided at the beginning of each step of the iteration, then the discretized momentum equation is solved leading to corrections for the velocity components and lastly the pressure correction equation is solved, correcting the initial pressure estimate. The algorithm then checks for convergence and either terminates the procedure at the desired convergence criteria or continues to the next iteration step.[16,37] The SIMPLE algorithm is already implemented in the open source CFD package OpenFOAM® for three dimensional laminar viscous flows and this implementation was utilized throughout the present study.

A schematic of the geometry and the coordinate system used is shown in Figure 1(a). Stream-wise wrinkles (sinusoidal riblets) are aligned in the direction parallel to the flow (z-direction) and are fully defined by two geometric parameters, the wavelength (λ) characterizing the spacing of the riblets and the amplitude (A), defined here as the distance between the peak and the trough of a wave as shown in Figure 1(b). Velocities in the x, y, z direction are denoted by u, v, w respectively and the total length of the plate along the flow direction is denoted by L. To compare simulations with different riblet geometries, two dimensionless groups are used: the aspect ratio $AR = 2A/\lambda$ of the riblets provides a local measure of the sharpness of the ribbed texture and λ/L provides a global measure of the size of the plate riblets with respect to the scale of the plate. Because the flow also evolves in the stream-wise direction it is also helpful in our analysis to compare the ridge wavelength to the local position using a local scaled variable z/λ. The lines $y = 0$ and $y = -A$ are chosen to be at the peak and trough of the wrinkles respectively and the surface of the riblets can then be written in the form $y_s = -\frac{A}{2} + \frac{A}{2}\cos\left(\frac{2\pi}{\lambda}x\right)$ where x is the cross-stream direction.

(a) (b)

FIG. 1. (a) Schematic of the 3D geometry of the flow domain used in OpenFOAM simulations; (b) The cross section of a wrinkled surface ($x - y$ plane)

The scale of the wrinkles simulated in this work were chosen based on the physical riblet sizes reported previously to show drag reduction[3,9,40–42]; the wavelength has been kept constant at $\lambda = 2\pi/3 \times 10^{-4}\ m \approx 200\ \mu m$ and the length of the domain ($0 < L/\lambda < 191$) and riblet amplitude ($AR = 0.48, 0.72, 0.95, 1.43, 1.91$) have been varied to investigate the effect of geometric changes on the level of drag reduction that can be achieved. The height of the domain has been kept constant to 1 mm and thus the surface area of the inlet and all the cross sections (in both smooth and riblet cases) is $2\pi \times 10^{-7}\ m^2$. To ensure the flow is laminar, the Reynolds number of all the cases simulated were limited to $Re_L < 5 \times 10^5$, which is the conventional criterion for natural (unforced) transition to turbulence on a flat

plate.[32]

The appropriate Reynolds number that parametrizes the relative importance of inertial and viscous effects in this spatially developing flow is defined using the flow direction (z) as the length scale (similar to the classical boundary layer theory) plus the maximum velocity of the free stream along the plate (W_∞), which is determined after the simulations are carried out. The local Reynolds number in this spatially-developing flow can thus be written as $Re_z = W_\infty z/\nu$, where $\nu = \mu/\rho$ is the kinematic viscosity of the fluid, μ is the dynamic viscosity and ρ is the density of the fluid.

The boundary conditions of this problem shown schematically in Figure 1(a) are similar to the case of a conventional boundary layer problem[32]. At the inlet (at the plane $z = 0$), flow enters the domain uniformly with uniform velocity W_{in} over the computational domain. The wrinkled surface at the bottom of the domain is non-permeable and acts as a no-slip wall, the upper surface has a zero pressure and no velocity gradient across it and the outlet (at the plane $z = L$) has zero velocity gradient across it and zero pressure. The two side walls have periodic boundary conditions. Note that due to leading edge effects, the maximum velocity in the simulations is up to 30% larger than the average inlet velocity W_{in} and this value of W_∞ is reported for each case studied throughout the paper.

A. Grid Resolution Study

The dimensions of the mesh elements used in this finite volume study have been kept similar for all cases, with an average size of $0.08 \times \lambda$. (The average size is calculated as the cubic root of average cell volume $V^{1/3}$). The smallest mesh elements are located close to the wall at the leading edge with an average size of $0.05 \times \lambda$ and the largest mesh element at the top boundary close to $z = L$ have a length scale in the stream-wise direction of $0.1 \times \lambda$. As an illustrative example of the problem size, to simulate the cases of $L/\lambda = 95.5$ with 3 wrinkles in the lateral direction, $N = 6.72{\times}10^6$ mesh elements were used. For longer/shorter geometries, the number of mesh elements was proportionally increased/decreased.

We first take two models with $AR = 1.91$ and $AR = 0$ (flat plate), $L/\lambda = 23.87$ and $Re_L = 6650$ and use these to investigate the effect of the spatial resolution by changing the number of cells (or changing the average size of the elements). The results are presented in Figure 2 in terms of the change in the overall integral drag coefficient on the plate as the number of elements N in the simulation is incremented, or as the characteristic size of the mesh element is reduced. The drag coefficient on the plate is defined as

$$C_D = \frac{D}{\frac{1}{2}\rho W_\infty^2 A_w} = \frac{1}{\frac{1}{2}\rho W_\infty^2 A_w} \int_{A_w} (\boldsymbol{\tau}_w . \boldsymbol{n}_w) . \mathbf{e}_z dA_w \tag{1}$$

where D is the total drag force on the wall, A_w is the wetted area of the wall, $\mathbf{n}_w$ is the local normal to the surface of the wall, $\boldsymbol{\tau}_w$ is the shear stress tensor evaluated at the wall. The total drag coefficient calculated using the Blasius solution $C_D = 1.328/\sqrt{Re_L}$ is also shown in Figure 2 by a dash-dotted line. Due to the leading edge effects present for plates at moderate Reynolds numbers (lower than $Re_L \lesssim 10^4$) the calculated results for this flat plate are about 20% higher than the classical Blasius theory. This difference can be captured using a higher order theory in which the drag coefficient includes an additional term and can be written as[32] $C_D = 1.328 Re_L^{-1/2} + 2.67 Re_L^{-7/8} + O(Re_L^{-1})$. The computational results are within 1% of this higher order theory.

Results show that increasing the number of elements in the finite volume model (FVM) from $1.22{\times}10^6$ to $1.68{\times}10^6$ (equivalently, changing the average cell size from 0.09λ to 0.08λ) changes the drag coefficient by only 0.1% and thus using the latter cell size gives sufficient resolution for the simulations. It is also clear from Figure 2 that the drag coefficient on the wrinkled plate (with $AR = 1.9$) is substantially lower than the flat plate, but it should be noted that this drag coefficient has been normalized by the total wetted area of the plate and does not explicitly display the increase in the surface area due to the presence of the riblets. The interplay of the reduced drag coefficient and the increase in the wetted surface

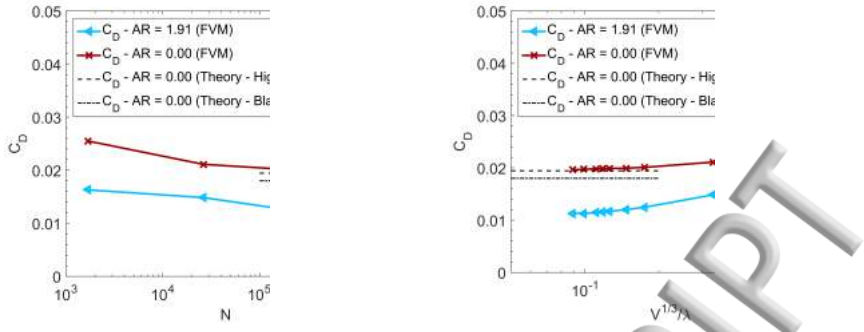

(a) (b)

FIG. 2. Effect of (a) the number of mesh elements and (b) the average size of the mesh elements on computed flow over surfaces with sinusoidal riblets. The results are presented for the calculated drag coefficient on the riblet walls for a geometry with $AR = 1.91$ and $AR = 0$ (flat plate), $Re_L = 6650$ and $L/\lambda = 23.87$. The theoretical results for a corresponding flat plate are shown with a dashed line (classical Blasius theory) and with a dash-dot line (higher order theory[32]).

area is discussed further in section III C. A similar average mesh size as the $N = 1.68 \times 10^6$ ($V^{1/3}/\lambda = 0.08$) cells used for $L/\lambda = 23.7$ has been employed throughout this study. For $L/\lambda = 47.75$ and $L/\lambda = 95.5$, $N = 3.36 \times 10^6$ and $N = 6.72 \times 10^6$ cells are used respectively.

B. Benchmark - Flat Plate Boundary Layer

As an initial benchmark, the problem of a flat plate boundary layer has been solved with the method outlined in section II. For this benchmark study the same geometry as Figure 1(a) has been used with a flat no-slip wall instead of the wrinkled one located at $y = 0$. The rest of the boundary conditions are the same as explained above. Water has been chosen as the working fluid with $\nu = 10^{-6}\ m^2/s$ and the inlet velocity is $W_{in} = 6\ m/s$. The corresponding maximum free-stream velocity is found to be $W_\infty = 6.56\ m/s$ and the Reynolds number based on the length is $Re_L = 31550$, corresponding to a flat plate of length $L = 0.1\ m$.

In order to validate the solution, the results from the numerical simulations are compared with the original laminar boundary layer theory. Based on the Blasius solution for the laminar boundary layer flow over a flat plate under zero pressure gradient, the velocity profiles along the length of the flat plate are self-similar when expressed in terms of a similarity variable η defined as $\eta = y/z\sqrt{Re_z}$. Using this rescaled wall variable η and non-dimensionalizing the velocity with the free-stream velocity w/W_∞, the velocity profiles collapse on each other, having the form shown by the solid line in Figure 3(a), as calculated by Blasius in 1907 [19,32]. The numerically computed velocity profile w/W_∞ at the end of the plate, $z = L$ (corresponding to $Re_L = 31550$) and scaled using the definition of $\eta = y/L\sqrt{Re_L}$ is also shown on Figure 3(a) by the points. As shown, the results of the theory and the numerical simulation match very well.

Additionally, the computed values of the wall shear stress along the plate can be compared with the Blasius boundary layer theory. According to the Blasius solution for the flat plate boundary layer, the shear stress at each point along the plate can be expressed in the form of a non-dimensional local skin friction coefficient C_f at each point on the flat wall and is given as[32]

$$C_f(z) = \frac{\tau_{yz}(y=0,z)}{\frac{1}{2}\rho W_\infty^2} = \frac{0.664}{\sqrt{Re_z}}. \tag{2}$$

The local skin friction distribution at the wall $\tau_{yz}(y = 0, z)$ is also extracted from the simulations, scaled with $1/2\ \rho W_\infty^2$ and plotted versus the local Reynolds number Re_z, next

to the theoretical line (solid line) in Figure 3(b). It is clear that good agreement with the Blasius result is obtained all along the plate.

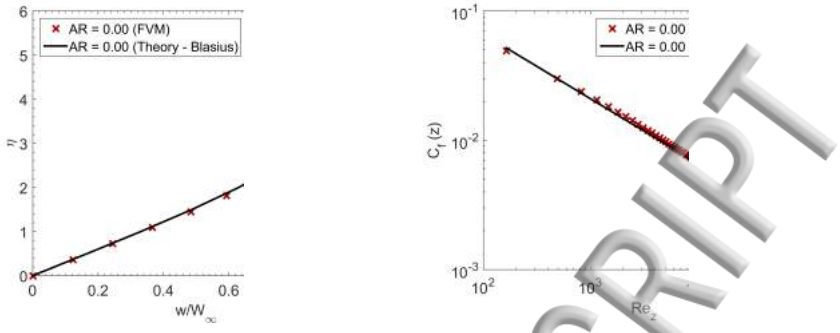

(a) (b)

FIG. 3. Results of finite volume modeling (FVM) of flat plate boundary layer using OpenFOAM and comparison with classical boundary layer theory for a flat plate with $Re_L = 31550$; (a) Velocity profile as a function of the similarity variable $\eta = y/z\sqrt{Re_z}$ at $z = L$. Maximum difference between the numerical calculations and the Blasius theory is 2.7%. (b) Distribution of skin friction coefficient $C_f(z)$ along the plate as a function of the local Reynolds number Re_z.

III. RESULTS

Having established the fidelity and convergence of our simulation technique we now proceed to use the finite volume code to investigate how the presence and shape of the sinusoidal riblet structures influence the development of the boundary layer flow. We first investigate the evolution of velocity profiles in the stream-wise and span-wise direction as well as the pressure distribution along the flow direction in section III A. Then we discuss different measures used to calculate the boundary layer thickness and how the riblets affect the evolution in the boundary layer thickness in section III B. Lastly, we examine the effect of the riblets on the shear stress distribution along the length of the plate as well as the total viscous drag acting on the surface in section III C and conclude whether drag reducing behavior can be observed.

A. Evolution of Velocity & Pressure Field

In contrast to the flat plate boundary layer, with a textured plate the velocity profile takes various shapes at each cross section depending on the span-wise (x-direction) location across the plate. As an example, the velocity profiles at 7 equi-spaced distances across a single sinusoidal wrinkle with $AR = 1.91$ at $Re_L = 13300$ and $L/\lambda = 47.75$ are presented in Figure 4. Similar shaped velocity profiles have been previously reported in both experimental and numerical simulations by Djenidi et al.[12,13] They reported velocity profiles, further away from the leading edge at a Reynolds number of $Re_L = 7.13 \times 10^4$ for a plate of $L/\lambda = 92$ featuring V-shaped grooves with $AR = 1.72$. Their profiles were comparable with the key features reported here, showing a retarded (nearly stagnant) flow inside the grooves (with a local velocity less than 20% of the free-stream velocity) while outside of the riblets all velocity profiles collapsed onto the same universal profile. Similar flow retardation and mean velocity profiles have been reported for turbulent flow over thin rectangular riblets as well as V-groove and U-groove textures of different sizes[15,18,29].

Because the differences in the shape of the velocity profiles vary systematically with the cross sectional position (x), the velocity profiles at the peak ($x = \lambda$) and in the trough ($x = \lambda/2$) of the wrinkles are chosen as the representative profiles to be discussed further as they

This manuscript was accepted by Phys. Fluids. Click here to see the version of record.

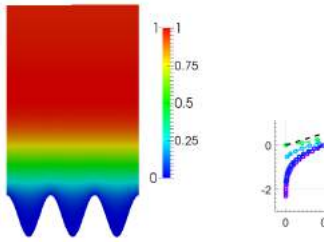

(a) (b)

FIG. 4. (a) Contours of dimensionless velocity and (b) velocity profiles $w(x,y)/W_\infty$ at 7 different locations of $x = i\lambda/6$ and $0 \leq i \leq 6$, within a single groove of a wrinkled plate with $AR = 1.91$ and $L/\lambda = 47.75$ at $Re_L = 13300$; Here $\eta = y/L\sqrt{Re_L}$ which is the same definition as used in the flat plate boundary layer theory. The dashed line denotes the theoretical profile from the Blasius solution to boundary layer equation for a flat plate ($AR = 0$).

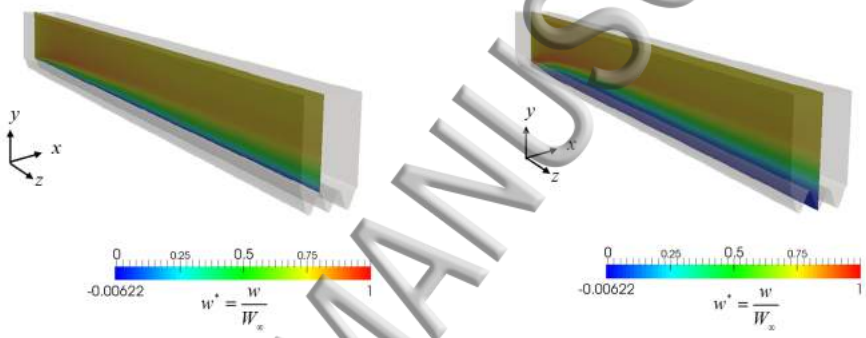

(a) (b)

FIG. 5. Schematic of the evolution in the boundary layer at (a) the peak ($x = \lambda$, $y_{min} = 0$) and (b) the trough ($x = \lambda/2$, $y_{min} = -A$) of a sinusoidal riblet surface with $Re_L = 13300$, $L/\lambda = 47.75$ and $AR = 1.91$.

present the two extrema of the problem. To illustrate qualitatively the three-dimensional evolution in the flow, contours of the dimensionless velocity distribution (w/W_∞) at the peak and trough for ribbed plates at $Re_L = 13300$, $L/\lambda = 47.75$ and $AR = 1.9$ are shown in Figures 5(a) and 5(b) respectively. Qualitatively the velocity contours at the peak appear very similar to the evolution observed along a flat plate boundary layer while the contour distribution in the trough differs from the peak and depict a thicker boundary layer for which most of the region inside the groove has velocities lower than 25% of the free-stream velocity.

The evolution in the velocity distributions can be studied more quantitatively by plotting the spatial changes of the velocity profiles in the flow direction, as shown in Figure 6. Here we non-dimensionalize the position along the plate using a characteristic diffusive scale ν/W_∞ so that the dimensionless position corresponds to a local Reynolds number $Re_z = W_\infty z/\nu$. Although the wrinkles (sinusoidal riblets) result in different velocity profiles at different locations, the main features and the local differences induced by the riblets can be effectively contrasted by comparing the velocity profiles at the peak and trough of a single riblet. Figures 6(a) and 6(b) present the velocity profiles at the peak and trough respectively (corresponding to the velocity contours in Figure 5). As we have noted, the stream-wise profiles at the peak, $w(x = \lambda, y)$ closely resemble the profiles of flat plate boundary layer theory. In the trough, the profiles $w(x = \lambda/2, y)$ look markedly different and reveal a thicker boundary layer, with the velocity inside the groove ($y < 0$) much lower than the free-stream velocity. For this case with $AR = 1.91$ the minimum velocity observed in each profile i.e. $w_{min} = \min(w(x = \lambda/2, y))$ is not always zero (as it is for the velocity

This manuscript was accepted by Phys. Fluids. Click here to see the version of record.

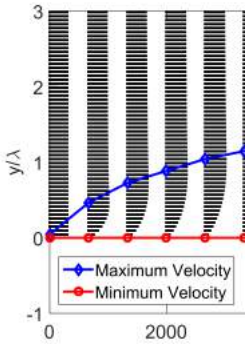

(a)

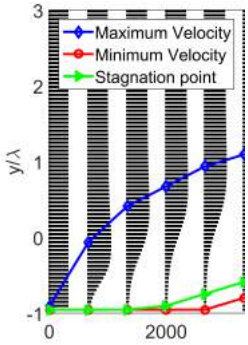

(b)

FIG. 6. Evolution of stream-wise velocity profiles $w(x, y, z)$ in the flow direction along (a) a peak $x = \lambda$ and $y_{min} = 0$ and (b) along a trough $x = \lambda/2$ and $y_{min} = -A$ of a surface with sinusoidal riblets with $L/\lambda = 47.75$ and $AR = 1.91$ at $Re_L = 13300$.

profiles at the peak $x = \lambda$), but can in fact become negative and within a region between about $2500 < Re_z < 10500$, a local *re-circulation* is observed. The location of the minimum velocity at each position z along the plate is shown in Figures 6(a) and 6(b) by the red circles joined by a line. If there is a *re-circulation* present, then the line of minimum velocity is displaced from the wall inside the groove. As a consequence above this line of points, a stagnation line is also formed inside the grooves and shown in each figure by the solid green line and triangular symbols.

At three representative local positions (corresponding to local Reynolds numbers of $Re_z = 4000$, 8000 and 12000) velocity profiles are extracted and plotted as shown in Figures 7. For $Re_z = 4000$ and $Re_z = 8000$ the trough profiles show a region of weak re-circulation inside the grooves ($y < 0$) whereas outside the groove, the velocity profiles at the peak and at the trough collapse on each other and evolve in similar fashion toward the outer inviscid flow far from the plate. Further along the plate at $Re_z = 12000$, the recirculating region ends, and thereafter the fluid inside the groove is in an essentially stagnant condition with zero velocity. Outside the groove the two velocity profiles meet and grow similarly to reach the free-stream velocity.

Our detailed computations of the velocity field in the vicinity of the sinusoidal texture reveal that due to the presence of the wrinkles the flow inside the grooves feels a strong retardation that ultimately results in this local re-circulating region. Eventually, as the frictional effects of the walls diffuse further outwards, the recirculating region ends and the fluid in the groove becomes almost stagnant inside the grooves. This stagnant fluid acts like a "cushion" of fluid on which the fluid outside of the grooves can slide. Similar behavior is

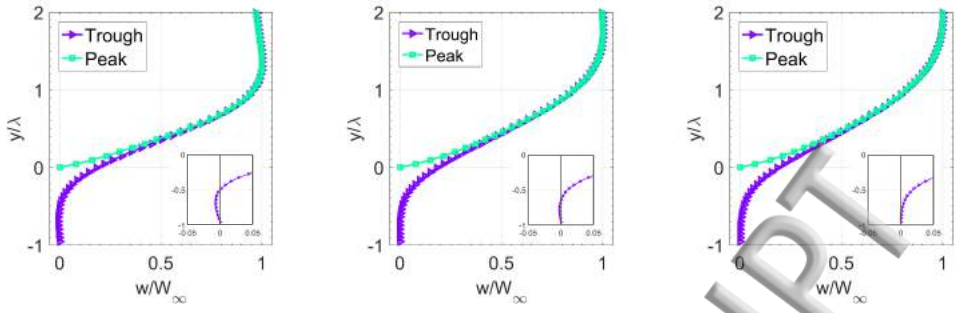

FIG. 7. Normalized velocity profiles at peak and trough at different locations (a)$Re_z = 4000, z/\lambda = 14.32$, (b)$Re_z = 8000, z/\lambda = 28.65$ and (c)$Re_z = 12000, z/\lambda = 42.97$ along the flow direction for a riblet surface with $AR = 1.91$ and $L/\lambda = 47.75$.

observed for cases with higher Reynolds numbers and longer lengths (achieved by changing the inlet velocity and the length of the plate). For example, for riblets of $AR = 1.91$ with global Reynolds number of $Re_L = 120600$ and $L/\lambda = 95.5$, velocity profiles in the trough are presented in Figure 8 and as it can be seen the re-circulation starts at a later position (i.e. a higher local Re_z) and it extends to a larger distance downstream.

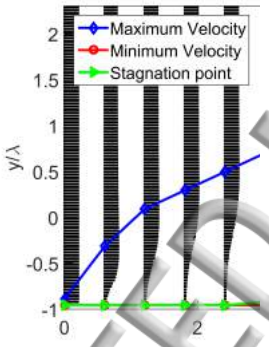

FIG. 8. Normalized velocity profiles along the flow direction in the trough of a wrinkle for $Re_L = 120600$, $L/\lambda = 95.5$ and $AR = 1.91$.

However, the aspect ratio AR of the wrinkles also has an effect on whether a re-circulating region is created or not. The progression of local velocity profiles for a wrinkled texture with global Reynolds number $Re_L = 13300$ and $L/\lambda = 47.75$ with a lower aspect ratio of $AR = 0.95$ (compared to $AR = 1.91$ in Figure 6(b)) is presented in Figure 9. Again we can see flow retardation inside the grooves with a stagnant layer of fluid and a bounding stagnation line, shown with a green line with triangular symbols. However for this shallower riblet geometry the minimum velocity is zero and located at the wall (shown by red line with circular symbols) and thus no re-circulation develops in the groove ($y < 0$).

This local re-circulation in the grooves can also be identified by using other vortex identification methods such as the scalar measure Q defined as $Q = \boldsymbol{\Omega} : \boldsymbol{\Omega} - \boldsymbol{S} : \boldsymbol{S}$.[21] This measure based on the the second invariant of the velocity gradient tensor, compares the rotation rate in the fluid (the anti-symmetric part of the velocity gradient tensor $\boldsymbol{\Omega} = \frac{1}{2}(\nabla \boldsymbol{u} - \nabla \boldsymbol{u}^T)$) with the irrotational straining (symmetric part of the velocity gradient tensor $\boldsymbol{S} = \frac{1}{2}(\nabla \boldsymbol{u} + \nabla \boldsymbol{u}^T)$) in the fluid.[21]. For example for $Re_L = 13300$ and $L/\lambda = 47.75$ the iso-Q surfaces of $Q = 1206.5 < \omega_{z,w} >^2$ are shown in Figure 10 where ω_z is the z component of the vorticity vector and $< \omega_{z,w} >$ is the magnitude of the mean z component of vorticity evaluated at

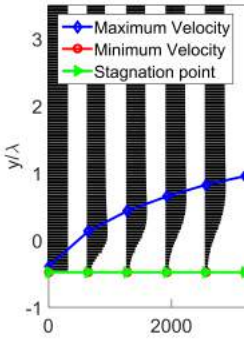

FIG. 9. Normalized velocity profiles along the flow direction in the trough of a wrinkle for $Re_L = 13300$, $L/\lambda = 47.75$ and $AR = 0.95$.

the wall. The observed vortical structures develop in the same region within the grooves as the local flow re-circulation that was observed in Figure 6(b).

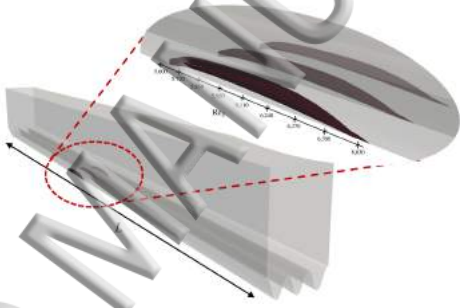

FIG. 10. Vortical structures in the grooves of a wrinkled surface for $Re_L = 13300$, $L/\lambda = 47.75$ and $AR = 1.91$ revealed by an iso-Q surface with $Q = 1206.5 < \omega_{z,w} >^2$; As seen in the figure the vortical structures are located in the middle of the re-circulating region identified in Figure 6(b).

Close to the leading edge of the plate, the effects of stream-wise pressure gradients are not negligible and this results in velocity profiles with a higher maximum velocity than the bulk fluid velocity W_{in} at the inlet[27,32]. To evaluate the effects of this local acceleration near the leading edge, the stream-wise pressure distribution above one of the troughs ($x = \lambda/2$) at $y = 0$ is shown in Figure 11. Figure 11(a) shows the dimensionless pressure distribution p^* (scaled as $p^* = p/\frac{1}{2}\rho W_\infty^2$) as a function of the local position along the plate (or local Reynolds number, Re_z) for a series of different aspect ratio wrinkles, keeping the inlet velocity constant. As seen in the figure, close to the leading edge a favorable pressure gradient (pressure decrease) is observed. However at an intermediate location along the plate this turns into an adverse pressure gradient (local stream-wise pressure increase) and ultimately the pressure increases to an asymptotic value of zero (set by the exit boundary condition).

In the case of the boundary layer over a flat plate ($AR = 0$), the changes in pressure disappear after $Re_z \approx 15000$, and from there onwards, the classical flat plate boundary layer approximation of $\frac{\partial P}{\partial z} \approx 0$ is a valid assumption to simplify the equations of motion. However, in the presence of the riblets, the region of favorable pressure gradient is extended and the pressure decreases to progressively lower values as the riblet aspect ratio increases. This results in the need for a larger pressure recovery in the adverse pressure gradient region, and this contributes to the establishment of local flow re-circulation. Comparing the case of $AR = 1.91$ from Figures 11(a) and 6(b) we can observe that the location of the minimum pressure is consistent with the location of the start of the re-circulation

inside the grooves. In addition the local region corresponding to the adverse pressure gradient ($\frac{\partial P}{\partial z} > 0$) corresponds to the entire recirculating region inside grooves. As the pressure gradient driving this re-circulating flow slowly decays away down the plate, a cushion of stagnant fluid is formed, which can be observed in the grooves in Figure 6(b). The computations in Figure 11(a) for different aspect ratios show that the pressure distribution in case of riblets with $AR \leq 0.95$ is only slightly different from $AR = 0$ (flat) case and thus results in only a very thin stagnant "cushion" of fluid. For this configuration this textured plate does not exhibit any re-circulation in the grooves (cf. Figure 8). However, for aspect ratios of $AR \gtrsim 0.95$ the magnitude of the local adverse pressure gradient is notably enhanced and the recirculating region shown in Figures 6(b) and 8 develops.

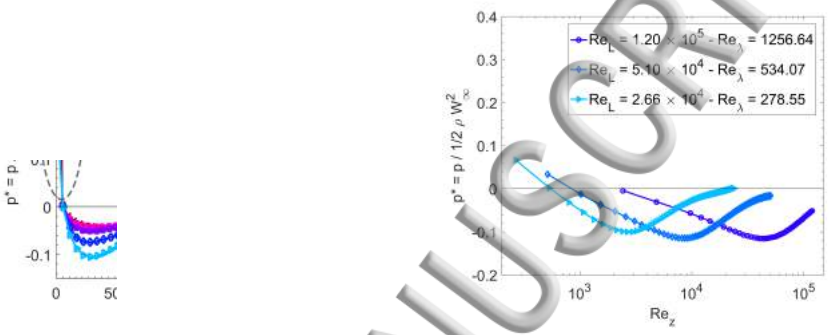

(a) (b)

FIG. 11. (a) Stream-wise pressure distribution at $x = \lambda/2$ and $y = 0$ (above a trough) as a function of the local Reynolds number down the plate for different aspect ratio riblets, keeping the inlet velocity constant ($Re_L = 25000$ and $L/\lambda = 95.5$). Inset shows additional details for small values of $Re_z < 10^3$ on a logarithmic scale. (b) Pressure distribution along the direction of flow on top of a groove at $y = 0$ for various inlet velocities (and different global Reynolds numbers) and $L/\lambda = 95.5$.

The evolution of similar pressure distribution can be calculated for the case of $AR = 1.91$ and $L/\lambda = 95.5$, and different global Reynolds numbers of 2.5×10^4, 5.1×10^4 and 2.5×10^5 (by changing the inlet velocity) and are presented as a function of the position or local Reynolds number in Figure 11(b). Comparing the three cases shows that the location of the minimum pressure (which coincides with the start of the recirculating region in the case of $AR = 1.91$) evolves with changes in the inlet velocity while the magnitude of the minimum dimensionless pressure stays nearly constant. We denote the location of the minimum pressure as L_c and seek to find a scaling for L_c as the flow geometry changes. Since the flow in the boundary layer close to the leading edge is quasi-steady and inertial pressure effects balance viscous stresses we expect that the pressure drop is of the same order as the divergence of the shear stress tensor in the z direction inside the grooves. A scaling estimate for the pressure gradient in this region gives

$$\frac{\partial p}{\partial z} \sim \frac{\rho W_\infty^2}{L_c} \tag{3}$$

and the divergence of the shear stress tensor in the z direction for the viscous flow inside the grooves (with characteristic groove length scale λ) can be expressed as

$$(\nabla . \boldsymbol{\tau})_z \sim \frac{1}{\lambda}\left(\frac{\mu W_\infty}{\lambda}\right). \tag{4}$$

Therefore for the pressure gradient to balance with the shear stress gradient inside the grooves, we require

$$\frac{\partial p}{\partial z} \sim (\nabla . \boldsymbol{\tau})_z \tag{5}$$

$$\frac{\rho W_\infty^2}{L_c} \sim \frac{1}{\lambda}\left(\frac{\mu W_\infty}{\lambda}\right) \tag{6}$$

$$L_c \sim \frac{\rho W_\infty \lambda^2}{\mu} \tag{7}$$

or in dimensionless form

$$\frac{L_c}{\lambda} \sim \frac{\rho W_\infty \lambda}{\mu} = Re_\lambda. \tag{8}$$

Therefore, the location of the minimum pressure along the plate is expected to increase linearly with increases in the inlet velocity. Figure 12 shows the calculated location of the minimum pressure for cases with inlet velocities $0.5 \leq W_{in} \leq 7\ m/s$ (and calculated maximum velocities of $0.6 \leq W_\infty \leq 8.2\ m/s$, respectively) for wrinkles with $AR = 1.91$ plotted as a function of $\rho W_\infty \lambda/\mu$. It can be seen from the figure that the calculated location scales linearly with the Reynolds number based on the wrinkle length scale (λ) $Re_\lambda = \rho W_\infty \lambda/\mu$ as predicted using the scaling above. Additional computations indicate that keeping the inlet velocity constant and varying the wavelength at a constant aspect ratio of $AR = 1.9$ results in the same scaling as Equation 8 and in Figure 12.

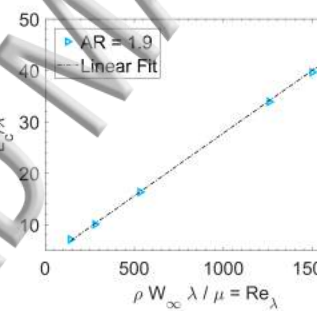

FIG. 12. Location of the minimum pressure for flow over textured surfaces with various inlet velocities $0.5 \leq W_{in} \leq 7\ m/s$ and the calculated maximum velocities of $0.6 \leq W_\infty \leq 8.2$ for $AR = 1.91$.

A principal goal of the present study is to investigate the source of friction reduction arising from variations in the texture of the surface. The local shear stress acting on the surface is directly proportional to the velocity gradient at the wall. Furthermore, as was seen earlier, the presence of the wrinkled topography provides a method to alter the curvature of the velocity profiles near the plate, especially inside the grooves, thus resulting in lower velocity gradients at the walls (for example, compare the peak and trough profiles in Figures 7). This results in a lower local wall shear stress inside the grooves compared with an equivalent flat plate and thus can result in a net reduction in the local average shear stress. This is especially seen in the recirculating region and stagnant areas where there is a cushion of almost stationary fluid. In these regions the velocity gradient is small or close to zero (as seen in Figure 6(b)). However, conversely, the total surface area of a grooved or ridged surface over which the shear stress is acting increases with the ridge scales and this can potentially offset or even overwhelm the local friction reduction. We therefore now proceed to carefully evaluate each contribution to the total skin friction on a wrinkled surface.

This manuscript was accepted by Phys. Fluids. Click here to see the version of record.

B. Boundary Layer Thickness & Velocity Decomposition

We have shown qualitatively in Figures 6, 8 and 9, that the presence of stream-wise sinusoidal riblets along the surface increases the overall thickness of the boundary layer. To quantify this, we need to develop an appropriate definition of the boundary layer thickness for flow over riblet surfaces. To do this we generalize the definition of displacement thickness for a two dimensional flat plate boundary layer to the integral form shown below[14,32]

$$\frac{\Delta^*}{z\ \alpha\lambda} = \frac{1}{z\ \alpha\lambda}\int_S \left(1 - \frac{w}{W_\infty}\right) dS \tag{9}$$

where Δ^* is now a *displacement area*, α is the number of wrinkles modelled in the simulation, z is the local stream-wise location and S is the cross sectional area of the flow in the $x-y$ plane. This expression for $\Delta^*(z)$ is defined locally but the equation can be extended to a global definition by replacing the position z with the total plate length L. The boundary layer thickness for a flat plate ($AR = 0$) and three different wrinkle textures of $AR = 0.48$, $AR = 0.95$ and $AR = 1.91$ are calculated for cases with various inlet velocities and a fixed $L/\lambda = 47.75$ and plotted on double logarithmic axes versus the global Reynolds number $Re_L = \rho W_\infty L/\mu$ in Figure 13. From the figure, it is clearly seen that increasing the aspect ratio of the riblets (AR) results in an increase in the thickness of the boundary layer, as expected from the velocity contours shown in figure 6.

At higher Reynolds numbers $Re_L > 10^4$ when the initial pressure gradient is negligible, the flat plate results extracted from the computations follow the $Re_L^{-0.5}$ scaling as calculated by Blasius. However, for lower Reynolds numbers, where the effects of the initial pressure gradient are non-negligible along the entire length of the plate, the data follows the scaling found from the higher order boundary layer theory results presented by van de Vooren and Dijkstra[36], which can be fitted to a power law proportional to $Re_L^{-0.44}$.

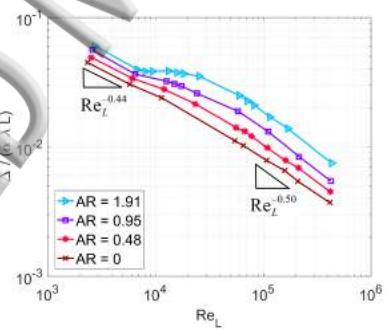

FIG. 13. Boundary layer thickness for different Re_L and different wrinkle aspect ratios; in all cases $L/\lambda = 47.75$ and for each profile the change in the Reynolds number is due to systematically changing the inlet velocity W_{in} which results in changes of the calculated maximum velocity W_∞.

In addition to the displacement area, a momentum area (the equivalent of the classical momentum thickness for a boundary layer that now varies in both x and y) can be calculated using the following expression[14,32]

$$\frac{\Theta}{z\ \alpha\lambda} = \frac{1}{z\ \alpha\lambda}\int_S \frac{w}{W_\infty}\left(1 - \frac{w}{W_\infty}\right) dS. \tag{10}$$

Similar to displacement area, the above definition is local and it can be extended to a global definition by replacing the position z with the length of the plate L.

Keeping the inlet velocity constant, the variation of the displacement area (Δ^*) and momentum area (Θ) locally along the flow direction (z) are plotted in Figure 14 for wrinkles

This manuscript was accepted by Phys. Fluids. Click here to see the version of record.

with various aspect ratios, showing an increase in the local displacement area of the boundary layer as AR increases. For all wrinkled cases studied this value is larger than for a flat plate with $AR = 0$ but the results slowly converge as Re_z increases beyond 10^4. This provides a clear indication that the effects of the wrinkled texture on the boundary layer size decay away as the flow progresses along the plate. In the case of the momentum area, again the local value of the momentum area for wrinkled walls is always larger than the flat wall, but as Re_z increases beyond 10^4, the data once again converges to the flat plate results.

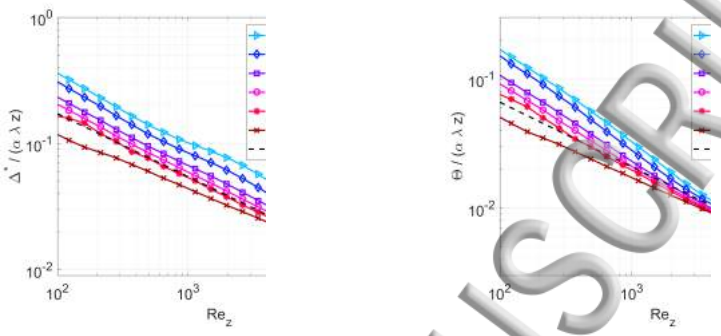

FIG. 14. Evolution of (a) the local displacement area (Δ^*) and (b) the local momentum area (Θ) along the plate (plotted in the form of a local Reynolds number Re_z) for wrinkles with different aspect ratios $0 < AR < 2$ keeping the length ($L/\lambda = 191$) and inlet velocity constant $W_{in} = 1\ m/s$. For these conditions, calculations for a flat plate ($AR = 0$) give $W_\infty = 1.33\ m/s$.

The shape factor $H = \Delta^*/\Theta$, is used frequently in aerodynamics as an indicator of boundary layer separation and re-circulation[5,14,32]. For flow over a flat plate in the laminar regime, $H < 2.65$ and at higher Reynolds numbers it reaches the value of $H = 2.65$ as given by the Blasius solution. The shape factor of the evolving boundary layer profiles along the length of the plates are shown in Figure 15 for wrinkles with different aspect ratios as a function of the local Reynolds number Re_z (corresponding to Figure 14). The introduction of stream-wise wrinkles results in an increase in the local shape factor of the viscous boundary layer and as the aspect ratio of the wrinkles progressively increases the shape factor H increases. This indicates a retardation in the local velocity close to the wall compared with the flat wall ($H < 4$)[14], but no re-circulation for $0 < AR < 1.5$. For the case with the highest aspect ratio ($AR = 1.91$), the shape factor reaches a peak value of $H = 4.5$ at $Re_z \sim 4000$ and then as the flow progresses along the plate H monotonically decays to a nearly constant value. The region with local Reynolds number of $3000 \leqslant Re_z \leqslant 8000$ where the shape factor goes through an increase and then a decrease corresponds to the re-circulation region documented earlier in Figure 6(b). At distances further down the plate the amplified value of the shape factor ($H > 2.65$) is a quantitative indication of fluid flowing over a cushion of stagnant fluid.

It is of interest to understand the differences between the calculated velocity profiles obtained for flow over wrinkled surfaces with different aspect ratios and the corresponding Blasius solution for the flat plate at every location of the riblet cross section. As we saw earlier, far from the surface of the riblets, the velocity profiles at different cross sectional locations collapse onto the same profile and behave similarly to the Blasius solution (Figure 4). Additionally, as we move further down the plate, the effects of the riblets on the velocity profile are confined to the creation of a cushion of stagnant fluid inside the grooves and are barely noticeable outside the grooves. In order to examine the difference between the classical two dimensional boundary layer and the current computations, the velocity contours at each cross section are decomposed into two additive contributions; the first contribution assumes the flat plate boundary layer solution of Blasius holds at every location in the cross section and is here denoted by $w_{BL}(x, y)$. The second contribution is obtained from the difference between the actual velocity profile $w(x, y)$ and the flat plate boundary

This manuscript was accepted by Phys. Fluids. Click here to see the version of record.

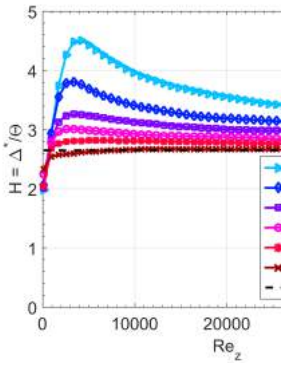

FIG. 15. Shape factor ($H = \Delta^*/\Theta$) of the velocity profile in a viscous boundary layer for different aspect ratio wrinkles corresponding to Figure 14.

layer solution at every cross sectional location, denoted by $\Delta w(x,y) = w(x,y) - w_{BL}(x,y)$; therefore:

$$\frac{w(x,y)}{W_\infty} = \frac{w_{BL}(x,y)}{W_\infty} + \frac{\Delta w(x,y)}{W_\infty}. \tag{11}$$

The velocity gradient and the shear stress (proportional to the velocity gradient at the wall or $n = 0$) can thus also be decomposed into two parts:

$$\frac{\partial w}{\partial n} = \frac{\partial w_{BL}}{\partial n} + \frac{\partial \Delta w}{\partial n} \quad \rightarrow \quad \tau = \tau_{BL} + \mu \frac{\partial \Delta w}{\partial n} \tag{12}$$

where τ_{BL} is the wall shear stress on the wrinkled wall, assuming the flat plate boundary layer solution holds at every location. This decomposition can be used to understand the increase or reduction in the local shear stress due to the periodic texture of the wall and illustrative examples of this decomposition are presented in Figures 16, 17 and 18. If the flat plate solution was the solution everywhere to the velocity field (w_{BL}), then the gradient of the velocity field normal to the wall (n) evaluated at the wall ($n = 0$ or $y = y_s$) could be found from the expression

$$\left.\frac{\partial w_{BL}}{\partial n}\right|_{n=0} = \sqrt{1 + \left(\tfrac{\pi A}{\lambda} \sin\left(\tfrac{2\pi}{\lambda} x\right)\right)^2} \left.\frac{\partial w_{BL,f}}{\partial y}\right|_{y=y_s} \tag{13}$$

where $w_{BL,f}$ is the Blasius solution on the flat plate. The shear stress at the wall is defined as $\tau = \mu\, \partial w/\partial n|_{n=0}$, thus

$$\tau_{BL} = \sqrt{1 + \left(\tfrac{\pi A}{\lambda} \sin\left(\tfrac{2\pi}{\lambda} x\right)\right)^2}\, \tau_{BL,f} \tag{14}$$

where $\tau_{BL,f}$ is the wall shear stress for the flat wall as calculated by the Blasius solution. Since the first trigonometric term in the expression in Equation 14 is always larger than or equal to unity, the shear stress at the wall of a textured surface (in this case a sinusoidally wrinkled surface) would be higher than that of the flat plate if the Blasius solution were to hold everywhere for flow over a riblet surfaces ($\tau_{BL} > \tau_{BL,f}$). Therefore, any local decrease in the shear stress on the wrinkled plate (compared with the flat plate) will be dependent on the sign of the last term in Equation 12. This decomposition can be used to explain how wrinkle size affects changes in the viscous shear stress compared to the stress distribution above a flat plate at the same local Reynolds number Re_z. For example the cross sectional

This manuscript was accepted by Phys. Fluids. Click here to see the version of record.

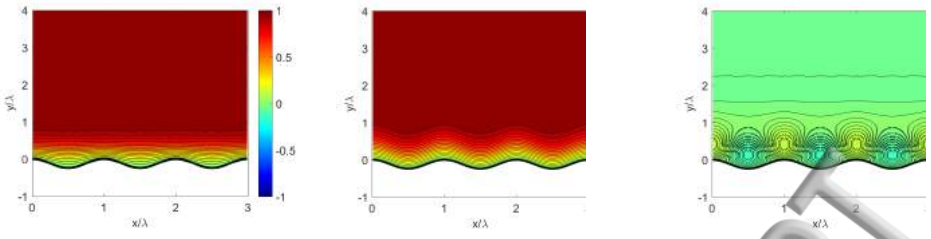

(a) (b) (c)

FIG. 16. Decomposition of the full computed velocity profile (w/W_∞) shown in (a) into two pieces; the first one shown in (b) is based on the flat plate boundary layer w_{BL}/W_∞ plus a velocity defect ($\Delta w/W_\infty$) shown in (c). Figures above shown for $Re_z = 4000$ and $z/\lambda = 14.32$ with $AR = 0.48$.

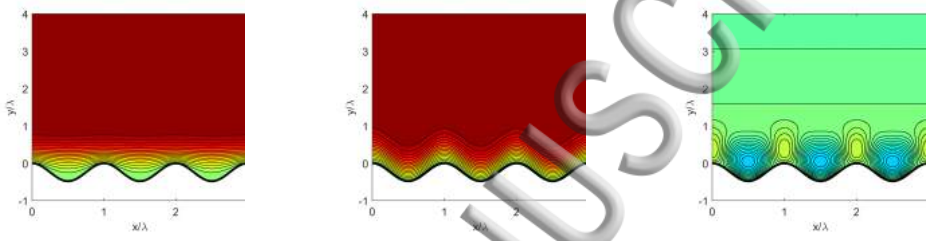

(a) (b) (c)

FIG. 17. Decomposition of the full computed velocity profile (w/W_∞) shown in (a) into two pieces; the first one shown in (b) is based on the flat plate boundary layer w_{BL}/W_∞ plus a velocity defect ($\Delta w/W_\infty$) shown in (c). Figures above are for $Re_z = 4000$ and $z/\lambda = 14.32$ with $AR = 0.95$.

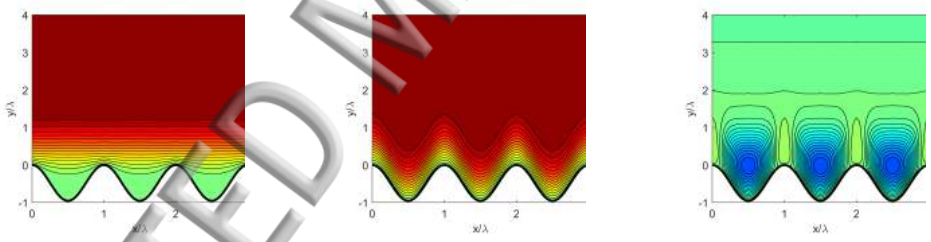

(a)w/W_∞ (b)w_{BL}/W_∞ (c)$\Delta w/W_\infty$

FIG. 18. Decomposition of the full computed velocity profile (w/W_∞) shown in (a) into two pieces; the first one shown in (b) is based on the flat plate boundary layer w_{BL}/W_∞ plus a velocity defect ($\Delta w/W_\infty$) shown in (c). Figures above are for $Re_z = 4000$ and $z/\lambda = 14.32$ with $AR = 1.91$.

velocity contours for three different wrinkle sizes ($AR = 0.48$, $AR = 0.95$ and $AR = 1.91$) with $Re_z = 4000$ and $z/\lambda = 14.32$ are shown in Figures 16, 17 and 18. In each case the wrinkles have the same wavelength while only the amplitude of the wrinkles is changed. In all the figures, the y direction is normalized with the constant wavelength (λ) of the wrinkle.

The most prominent differences between the actual velocity profiles shown in Figures 16(a), 17(a) and 18(a) and the locally-shifted form of the Blasius solution w_{BL} (Figures 16(b), 17(b) and 18(b)) is inside the grooves where the velocity boundary layer is thicker and the flow is almost stagnant close to the wall (as was also demonstrated earlier). Therefore, the velocity defect Δw (shown in Figures 16(c), 17(c) and 18(c)) shows non-zero and negative values which results in a lower velocity gradient in the grooves compared with $\partial w_{BL}/\partial n|_{n=0}$ inside the grooves. Another region of difference is at the peak of the riblets. Here the difference is not as clearly discernible, but is clearly non-zero and yields positive values of the velocity defect Δw (with magnitudes lower than those observed inside the grooves). This results in a slightly higher velocity gradient at the peak of the riblets

compared to $\partial w_{BL}/\partial n$. The combination of these features results in a substantially lower local shear stress inside the grooves, plus a slightly higher shear stress at the peak of the riblets. Similar conclusions have been reported previously (through DNS results as well as experiments) indicating that the velocity gradients, and thus local shear stress, observed at the peaks and troughs of riblet structures are higher and lower respectively than the results for the flat plate.[10,20,23]

Based on Equation 14 an increase in the aspect ratio ($AR = 2A/\lambda$) of the wrinkles would result in an increase in the wall shear stress calculated by using just the Blasius solution for the riblets (τ_{BL}) without correction. However when examining the actual velocity defect structure in Figures 17(c), 16(c), and 18(c) we see a stronger negative velocity gradient inside the grooves which, from Equation 12, can result in a reduction in the net local shear stress evaluated at each cross section along the plate.

C. Wall Shear Stress and Drag

Finally, we investigate the ability of the riblets to reduce the total drag force exerted on the wall. To do this we evaluate the average skin friction coefficient C_f (Figure 19(a)) and the total integrated drag force D (Figure 19(b)) with respect to the flat surface. We consider cases with different aspect ratios ($0 < AR < 2$) and constant $L/\lambda = 47.75$, as a function of the global Reynolds number Re_L (by using different inlet velocities W_{in} and computing the maximum calculated velocity W_∞) for each case. If the stress tensor at the wall and local wall normal vector evaluated at a position x_s, y_s on the riblet surface are defined as $\boldsymbol{\tau}_w(x_s, y_s; z)$ and $\boldsymbol{n}_w(x_s, y_s; z)$ respectively (where $y_s = -\frac{A}{2} + \frac{A}{2}\cos(\frac{2\pi}{\lambda}x_s)$), then the total drag force on a plate of length L and the average skin friction coefficient are defined as

$$D = \int_0^L [\ \boldsymbol{\tau}_w(x_s, y_s; z).\boldsymbol{n}_w(x_s, y_s; z)\ ].\boldsymbol{e}_z\ dA_w \tag{15}$$

and

$$C_f = \frac{D}{\frac{1}{2}\rho W_\infty^2\ A_w} \tag{16}$$

respectively, where A_w is the wetted area of the riblet wall. A reduction in the skin friction coefficient is defined as $\Delta C_f = C_f - C_{f,0}$ where $C_{f,0}$ is the skin friction coefficient of a flat plate and the reduction in total drag is defined as $\Delta D = D - D_0$ where D_0 is the total drag on the flat surface. Note that negative values in both plots correspond to skin friction coefficient reduction and drag reduction respectively. The results in Figure 19 show that the presence of the riblets reduces the average skin friction coefficient on the wall in nearly all of the riblet cases considered. At the same value of the global Reynolds number (Re_L) increasing the aspect ratio (AR) results in a progressively larger decrease in the average skin friction coefficient. This also confirms our observations based on consideration of the velocity decomposition that the negative velocity defect observed inside the grooves (Figures 16(c), 17(c) and 18(c)) results in a reduction in the average shear stress compared to the flat plate. As the aspect ratio of the wrinkles increases, the increase in the magnitude of the negative velocity defect $\Delta w < 0$ results in a higher reduction in the average skin friction coefficient.

However, reduction of the average skin friction coefficient alone cannot define whether a textured riblet surface is drag reducing or not because the total area of the wetted surface is also increased through the presence of the wrinkles. The total wetted surface area of the textured plate is larger than a flat surface and increases with AR; thus for a textured surface to be drag reducing the reduction in the skin friction coefficient due to the riblets must more than offset the increasing wetted area. For the results shown in Figure 19(b) at $L/\lambda = 47.75$ the only cases that appear to show a net drag reduction are the cases with aspect ratios of $AR = 0.48$ and $AR = 0.95$ and global Reynolds number of $Re_L = 13300$.

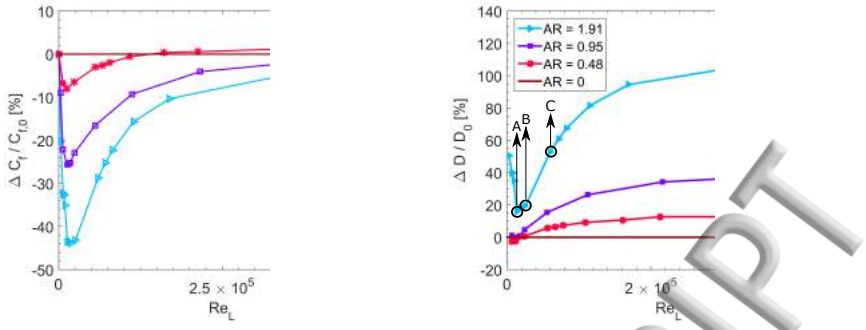

FIG. 19. Reduction in (a) the skin friction coefficient (C_f) and (b) changes in the total drag (D) for wrinkles of different aspect ratios, fixed plate length $L/\lambda = 47.75$ and different Re_L (varying the inlet velocity). Points A, B and C correspond to the same points shown below in Figure 21(b).

The rest of the cases show substantial increase in the total drag when compared to an equivalent flat surface.

To better understand these drag reducing cases and how changes in the length of the plate (Re_L) and aspect ratio (AR) interact to affect the total drag, we consider the following situations: we keep the inlet velocity constant (thus keeping W_∞ constant) and extend our calculations to plates of longer total lengths than those used in the computations presented in Figure 19. We consider a maximum plate length of $L/\lambda = 191$ and an inlet velocity of $W_{in} = 1\ m/s$ (thus corresponding to a maximum global Reynolds number of $Re_L = 5\times10^4$) for 5 different aspect ratios of $0 < AR < 2$. The results are shown in Figure 20. We first consider the distribution of the wall shear stress on the wall as a function of different aspect ratios at different positions z along the length of the plate corresponding to different values of the local Reynolds number, Re_z. From steady two-dimensional boundary layer theory we know that the local shear stress on the wall decreases along the plate as $\tau_{BL} \sim Re_z^{-1/2}$ (Equation 2). For reference we therefore plot this result as the black dashed line in Figure 20(a). For a ribbed plate, the wall shear stress is now a function of lateral position x_s, y_s on the surface as well as distance down the plate. We therefore define the dimensionless local average shear stress distribution at any distance z along the plate as

$$\tau^*(z) = \frac{1}{\frac{1}{2}\rho W_\infty^2}\frac{1}{l_C}\int_C \boldsymbol{\tau}_w(x_s, y_s; z).\boldsymbol{n}_w(x_s, y_s; z).\boldsymbol{e}_z\ dl \tag{17}$$

where C is the riblet contour at each stream-wise cross section, l_C is the total length of the riblet contour ($l_C = \int_C dl$) and dl is the line element along the rib transverse to the flow direction. In Figure 20(a) we show the evolution in the local average shear stress along the length of the plate for wrinkled cases with $0 < AR < 2$ and plates with $Re_L = 4 \times 10^4$ and $L/\lambda = 191$ compared with the shear stress on the flat plate. It is clear that the presence of the wrinkles changes the evolution in the shear stress distribution along the flow direction. As seen in this figure, close to the leading edge of the plate, the presence of wrinkles does not reduce the large initial shear stress that results from the sudden generation of vorticity at the leading edge. However as the local Reynolds number Re_z increases along the plate, the wrinkles retard the flow in the grooves and thus reduce the local average shear stress at the wall. The case of $AR = 1.91$ shows a region with almost constant average shear stress between $5000 < Re_z < 12000$ which also corresponds with the re-circulation region presented earlier in Figure 6(b). Smaller aspect ratios do not show any re-circulation and thus there is no region with constant shear stress distribution.

At lower local Reynolds numbers $Re_z \leqslant 10^3$ (close to the leading edge), the local average shear stress for all the riblet cases is nearly the same as the shear stress distribution on the flat plate. However, as we established above, increasing the aspect ratio of the riblets

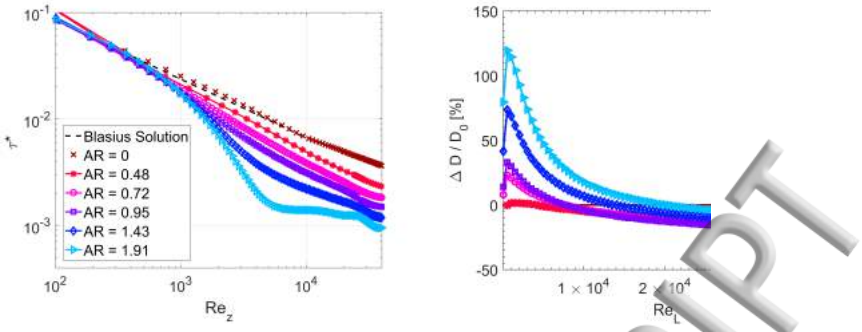

(a) (b)

FIG. 20. (a) Evolution of the local transverse average of dimensionless wall shear stress distribution (Equation 17) for the same inlet velocity and different aspect ratio riblets. (b) Increases ($\Delta D > 0$) and reductions ($\Delta D < 0$) in the total drag force (D) for wrinkled plates of different total length of the range $0 < L/\lambda < 191$ (increasing global Reynolds number Re_L) for various aspect ratio wrinkles $0 < AR < 2$, keeping the wavelength λ constant.

results in an increase in the wetted area and therefore this results in a substantial increase in the total drag for plates with $AR > 0.48$ and global Reynolds numbers of $Re_L < 8000$ (and nearly no change in the total drag for the case of $AR = 0.48$). However, further down the plate, as the cushion of stagnant fluid starts to form inside the grooves, the reduction in the local shear stress can offset the increase in the wetted area and this results in a net reduction of the total drag.

As we show in Figure 20(b) it becomes clear that riblets have the potential of reducing drag provided the plate is *longer* than a minimum critical length $Re_{L,c}(AR)$ (which can be determined from where each of the curves cross the value of zero on the ordinate axis). Secondly, the sharpness of the riblets plays an important role in controlling the extent of total drag reduction achieved. Higher aspect ratio wrinkles provide greater local shear stress reduction but this is offset by the large increase in wetted area for very high aspect ratios. For the range of global Reynolds number Re_L we have studied, the case with $AR = 0.95$ was found to provide the highest reduction in the total drag. We can illustrate this most clearly by holding the global Reynolds number Re_L and riblet spacing L/λ constant and calculating the total drag reduction as a function of the aspect ratio of the riblets. We illustrate this in Figure 21(a) for three different values of Re_L showing that for each of the cases there is an optimum aspect ratio providing the largest possible drag reduction. Quite generally we find that the total frictional drag reduction (corresponding to $\Delta D/D_0 < 0$) at a constant global Reynolds number Re_L and L/λ is first enhanced as the aspect ratio of the wrinkles increases, then reaches an optimum and as the aspect ratio increases still further the extent of drag reduction decreases and eventually shifts to a net drag increase. For $Re_L > 10^4$ the optimum aspect ratio is slightly less than unity, but after that the optimum aspect ratio is close to $AR \approx 1$. Previous wind tunnel experiments by Walsh with V-groove riblets of $AR = 1$ and $AR = 2$ at constant free-stream velocity also show that riblets with $AR = 1$ result in a larger drag reduction compared to $AR = 2$.[39]

A similar trend as discussed above can be observed for the other data points presented in Figure 19(b) as the plate length is increased. To illustrate that, at a constant aspect ratio of $AR = 1.9$ (which did not show any drag reduction for the case of $L/\lambda = 47.75$) the evolution in the total drag force for plates of various lengths ($1 < L/\lambda < 191$) with different inlet velocities are presented in Figure 21(b). As we discussed in section III A, changing the inlet velocity results in a change in the pressure distribution (Figure 11(b)) and thus alters the location of the minimum pressure inside the grooves (Figure 12). For short plates, the presence of the wrinkles leads to an overall increase in the frictional drag, but in each case a net drag reduction is observed when the length of the plate exceeds a critical value. However, due to the differences in the pressure distribution among the cases with different inlet velocities, the cross over from drag increase to drag decrease occurs at

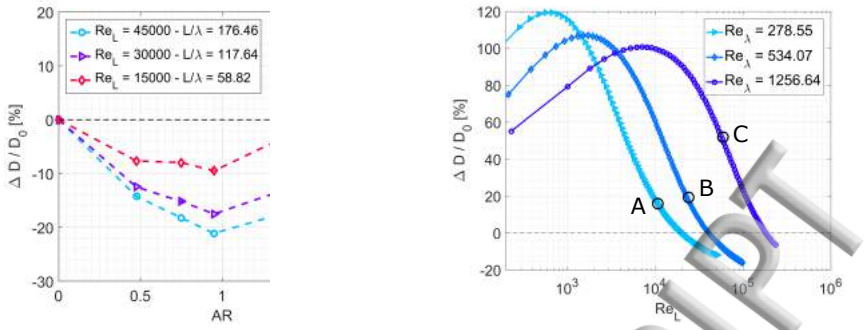

FIG. 21. (a) Drag reduction curve for plates with global Reynolds number of $Re_L = 15000$ and plate length $L/\lambda = 58.82$, global Reynolds number $Re_L = 30000$ and plate length $L/\lambda = 117.64$, and global Reynolds number $Re_L = 45000$ and plate length $L/\lambda = 176.46$ (same inlet velocity $W_{in} = 1\ m/s$ and the same wavelength $\lambda = 2\pi/3 \times 10^{-1}\ mm$) as a function of the aspect ratio of the riblets. (b) Reduction in total drag for wrinkled plates of different length Re_L, $AR = 1.9$ and inlet velocities of $W_{in} = 1, 2$ and $5\ m/s$ corresponding to $Re_\lambda = 278.55,\ 534.07$ and 1256.64. Points A, B and C correspond to the same points in Figure 19(b).

a longer plate length as the free-stream velocity (and thus Re_λ) is increased. Points A, B and C indicated on the figure correspond to the points A, B and C noted in figure 19(b) ($Re_L = 1 \times 10^4,\ 2.4 \times 10^4$, and 5.9×10^4 respectively) where for a fixed plate length of $L/\lambda = 47.75$ only a net drag increase was observed.

IV. CONCLUSIONS

In this paper we have examined in detail the effects of sinusoidal riblets on the structure and evolution of a steady viscous boundary layer. The presence of the riblets results in a local flow retardation inside the valleys of the riblets and even the possibility of a local flow reversal. Riblets increase the average thickness of the boundary layer as well, resulting in an increase in the shape factor of the boundary layer. The presence of riblets also change the pressure distribution close to the leading edge of the plate when compared with the flat boundary layer. This flow retardation creates a cushion of almost stagnant fluid inside the riblets upon which the fluid flowing above the plate can slide. This creates a non-uniform shear stress distribution laterally across the plate and a local average shear stress lower than the corresponding flat plate. For sufficiently long plates, this can result in a reduction of the total viscous drag force acting on the surface compared with flat surfaces, provided the aspect ratio of the wrinkles is not so large that the increase in wetted area offsets the local reduction in wall shear stress $\tau_w(x_s, y_s)$. By careful computation of the local skin friction coefficient $C_f(x_s, y_s)$ as well as the total integrated frictional drag force D we have shown that the reduction in drag is a function of the aspect ratio of the riblets. For each Re_L and L/λ there is an optimum aspect ratio where the highest drag reduction can be achieved. For fully developed viscous boundary layers at $Re_L \gtrsim 10^4$ (so that leading edge effects are not important), it appears that aspect ratios of order unity produce the maximum reduction in drag, which can be as large as $\Delta D/D_0 \approx -20\%$ at $Re_L \approx 4 \times 10^4$.

These detailed computations help rationalize why previous experimental measurements have reported conflicting conclusions regarding drag increases or decreases and will provide guidance for selecting optimal riblet sizes and spacings for specific design applications requiring minimized frictional drag.

ACKNOWLEDGMENTS

This research was supported by the Center for Clean Water and Clean Energy at MIT and KFUPM.

[1]Bacher, E. and Smith, C., "Turbulent boundary-layer modification by surface riblets," AIAA Journal **24**, 13821385 (1985).
[2]Bechert, D., Bruse, M., and Hage, W., "Experiments with three-dimensional riblets as an idealized model of shark skin," Experiments in Fluids **28**, 403–412 (2000).
[3]Bechert, D., Bruse, M., Hage, W., Van der Hoeven, J. T., and Hoppe, G., "Experiments on drag-reducing surfaces and their optimization with an adjustable geometry," Journal of Fluid Mechanics **338**, 59–87 (1997).
[4]Bechert, D., Hoppe, G., and Reif, W.-E., "On the drag reduction of the shark skin," in *1985 AIAA Shear Flow Control Conference* (1985).
[5]Blackwell, J. A., "Preliminary study of effects of reynolds number and boundary-layer transition location on shock-induced separation," NASA-TN-D-5003 (1969).
[6]Chan, E. P., Smith, E. J., Hayward, R. C., and Crosby, A. J., "Surface wrinkles for smart adhesion," Advanced Materials **20**, 711716 (2008).
[7]Chen, X. and Hutchinson, J. W., "Herringbone buckling patterns of compressed thin films on compliant substrates," Journal of Applied Mechanics **71**, 597 (2004).
[8]Choi, H., Moin, P., and Kim, J., "Direct numerical simulation of turbulent flow over riblets," Journal of Fluid Mechanics **255**, 503–539 (1993).
[9]Choi, K., Gadd, G., Pearcey, H., Savill, A., and Svensson, S., "Tests of drag-reducing polymer coated on a riblet surface," Applied Scientific Research **46**, 209–216 (1989).
[10]Chu, D. C. and Karniadakis, G. E., "A direct numerical simulation of laminar and turbulent flow over riblet-mounted surfaces," Journal of Fluid Mechanics **250**, 1–42 (1993).
[11]Dinkelacker, A., Nitschke-Kowsky, P., and Reif, W.-E., "On the possibility of drag reduction with the help of longitudinal ridges in the walls," in *Turbulence Management and Relaminarisation* (Springer, 1988) pp. 109–120.
[12]Djenidi, L., Liandrat, J., Anselmet, F., and Fulachier, L., "Numerical and experimental investigation of the laminar boundary layer over riblets," Applied Scientific Research **46**, 263–270 (1989).
[13]Djenidi, L., Squire, L., and Savill, A., "High resolution conformal mesh computations for V, U or L groove riblets in laminar and turbulent boundary layers," in *Recent Developments in Turbulence Management* (Springer, 1991) pp. 65–92.
[14]Drela, M., *Flight vehicle aerodynamics* (MIT Press, 2014).
[15]El-Samni, O., Chun, H., and Yoon, H., "Drag reduction of turbulent flow over thin rectangular riblets," International Journal of Engineering Science **45**, 436–454 (2007).
[16]Ferziger, J. H. and Peric, M., *Computational Methods for Fluid Dynamics* (Springer Science & Business Media, 2012).
[17]Furuya, Y., Nakamura, I., Miyata, M., and Yama, Y., "Turbulent boundary-layer along a streamwise bar of a rectangular cross section placed on a flat plate," Bulletin of JSME **20**, 315322 (1977).
[18]Goldstein, D., Handler, R., and Sirovich, L., "Direct numerical simulation of turbulent flow over a modeled riblet covered surface," Journal of Fluid Mechanics **302**, 333–376 (1995).
[19]Hager, W., "Blasius: A life in research and education," Experiments in Fluids **34**, 566–571 (2003).
[20]Hooshmand, D., Youngs, R., Wallace, J., and Balint, J., "An experimental study of changes in the structure of a turbulent boundary layer due to surface geometry changes," in *AlAA 21st Aerospace Sciences Meeting*, 83-0230 (American Institute of Aeronautics and Astronautics, 1983).
[21]Hunt, J. C., Wray, A. A., and Moin, P., "Eddies, streams, and convergence zones in turbulent flows," Studying Turbulence Using Numerical Simulation Databases-I1 , 193 (1988).
[22]Kennedy, J. F., Hsu, S.-T., and Lin, J.-T., "Turbulent flows past boundaries with small streamwise fins," Journal of the Hydraulics Division **99** (1973).
[23]Khan, M., "A numerical investigation of the drag reduction by riblet-surfaces," in *4th Joint Fluid Mechanics, Plasma Dynamics and Lasers Conference*, 86-1127 (AIAA, 1986).
[24]Kim, H., Kline, S., and Reynolds, W., "The production of turbulence near a smooth wall in a turbulent boundary layer," Journal of Fluid Mechanics **50**, 133 (1971).
[25]Kim, J., Moin, P., and Moser, R., "Turbulence statistics in fully developed channel flow at low Reynolds number," Journal of Fluid Mechanics **177**, 133166 (1987).
[26]Lee, S.-J. and Lee, S.-H., "Flow field analysis of a turbulent boundary layer over a riblet surface," Experiments in Fluids **30** (2001), 10.1007/s003480000150.
[27]Narasimha, R. and Prasad, S., "Leading edge shape for flat plate boundary layer studies," Experiments in fluids **17**, 358–360 (1994).
[28]Neumann, D. and Dinkelacker, A., "Drag measurements on V-grooved surfaces on a body of revolution in axial flow," Applied Scientific Research (1991), 10.1007/BF01998668.
[29]Park, S.-R. and Wallace, J. M., "Flow alteration and drag reduction by riblets in a turbulent boundary layer," AIAA Journal **32**, 31–38 (1994).
[30]Patankar, S. V. and Spalding, D. B., "A calculation procedure for heat, mass and momentum transfer in three-dimensional parabolic flows," International Journal of Heat and Mass Transfer **15**, 1787–1806 (1972).

[31]Raayai-Ardakani, S., Yague, J. L., Gleason, K. K., and Boyce, M. C., "Mechanics of graded wrinkling," Journal of Applied Mechanics **83** (2016), 10.1115/1.4034829.
[32]Schlichting, H., Gersten, K., and Gersten, K., *Boundary-layer theory* (Springer, 2000).
[33]Simpson, R. L., *An investigation of the spatial structure of the viscous sublayer* (Max-Planck-Institut für Strömungsforschung, 1976).
[34]Tardu, S. F., "Coherent structures and riblets," Applied Scientific Research **54**, 349385 (1995).
[35]Terwagne, D., Brojan, M., and Reis, P., "Smart morphable surfaces for aerodynamic drag control," Advanced Materials **26**, 66086611 (2014).
[36]Van De Vooren, A. and Dijkstra, D., "The Navier-Stokes solution for laminar flow past a semi-infinite flat plate," Journal of Engineering Mathematics **4**, 9–27 (1970).
[37]Versteeg, H. and Malalasekera, W., *An Introduction to Computational Fluid Dynamics* (Pearson, 1995).
[38]Viswanath, P., "Aircraft viscous drag reduction using riblets," Progress in Aerospace Sciences **38**, 571600 (2002).
[39]Walsh, M., "Drag characteristics of V-groove and transverse curvature riblits," in *Symposium on Viscous flow drag reduction* (AIAA Prog. Astronaut. Aeronaut., 1980).
[40]Walsh, M. and Lindemann, A., "Optimization and application of riblets for turbulent drag reduction," in *22nd Aerospace Sciences Meeting* (American Institute of Aeronautics and Astronautics, 1984) p. 347.
[41]Walsh, M. J., "Riblets as a viscous drag reduction technique," AIAA journal **21**, 485–486 (1983).
[42]Walsh, M. J., *Viscous drag reduction in boundary layers*, edited by D. M. Bushnell, Vol. 1 (AIAA, 1990) Chap. Riblets, pp. 203–261.
[43]Walsh, M. J. and Weinstein, L., "Drag and heat-transfer characteristics of small longitudinally ribbed surfaces," AIAA Journal **17**, 770771 (1979).
[44]Wen, L., Weaver, J., and Lauder, G., "Biomimetic shark skin: design, fabrication and hydrodynamic function," The Journal of Experimental Biology **217**, 16561666 (2014).
[45]Yin, J., Yage, J. L., Eggenspieler, D., Gleason, K. K., and Boyce, M. C., "Deterministic order in surface microtopologies through sequential wrinkling," Advanced Materials **24**, 54415446 (2012).